Research Square

Preprints are preliminary reports that have not undergone peer review.
They should not be considered conclusive, used to inform clinical practice,
or referenced by the media as validated information.

Coordination–Hydrodynamic Synergy Enables Efficient and Scalable Sky-Blue Perovskite Light-Emitting Diodes

Xiaoyang Guo

guoxy@ciomp.ac.cn

Changchun Institute of Optics, Fine Mechanics and Physics, Chinese Academy of Sciences

Longxiang Yang

Changchun institute of optics, fine mechanics and physics

Kai Sun

South China Normal University

Yafang Ren

Beijing Institute of Technology

Ying Lv

Changchun institute of optics, fine mechanics and physics

Tienan Wang

Changchun Institute of Optics, Fine Mechanics and Physics, Chinese Academy of Sciences

Jiang Wu

Changchun Institute of Applied Chemistry, Chinese Academy of Sciences

Yanheshig Ba

Changchun Institute of Optics, Fine Mechanics and Physics, Chinese Academy of Sciences

Xingyuan Liu

Changchun Institute of Optics, Fine Mechanics and Physics https://orcid.org/0000-0002-9681-1646

Article

Keywords:

Posted Date: November 20th, 2026

DOI: https://doi.org/10.21203/rs.3.rs-11591320/v1

License: This work is licensed under a Creative Commons Attribution 4.0 International License.
Read Full License

Additional Declarations: There is no conflict of interest

Coordination–Hydrodynamic Synergy Enables Efficient and Scalable Sky-Blue Perovskite Light-Emitting Diodes

Longxiang Yang[1,2,†], Kai Sun[4,†], Xiaoyang Guo[1,], Yafang Ren[5], Ying Lv[1], Tienan Wang[1], Jiang Wu[3,*], Bayanheshig[6], Xingyuan Liu[1,*]*

1. State Key Laboratory of Luminescence Science and Technology, Changchun Institute of Optics, Fine Mechanics and Physics, Chinese Academy of Sciences, Changchun 130033, P. R. China

2. University of Chinese Academy of Sciences, Beijing 100049, P. R. China

3. State Key Laboratory of Polymer Science and Technology, Changchun Institute of Applied Chemistry, Chinese Academy of Sciences, Changchun 130022, P. R. China

4. Institute for Advanced Materials & Guangdong Provincial Key Laboratory of Optical Information Materials and Technology South China Academy of Advanced Optoelectronics South China Normal University Guangzhou 510006, China.

5. Beijing Institute of Technology, Beijing 100081, P. R. China

6. National Engineering Research Center for Diffraction Gratings Manufacturing and Application, Changchun Institute of Optics, Fine Mechanics and Physics, Chinese Academy of Sciences, Changchun 130033, P. R. China

†These authors contributed equally: *Longxiang Yang, Kai Sun*

Corresponding author: Xiaoyang Guo (guoxy@ciomp.ac.cn); Jiang Wu (r_wuj33@ciac.ac.cn); Xingyuan Liu (liuxy@ciomp.ac.cn)

Keywords: blue perovskite light-emitting diodes, large-area devices, ternary co-solvent engineering, Marangoni flow balancing, coordination regulation

Abstract text

Although perovskite light-emitting diodes (PeLEDs) have achieved external quantum efficiencies (EQEs) exceeding 25% for red, green, and blue emission, realizing high efficiency together with large-area film uniformity remains a critical challenge for solution-processed devices. This difficulty arises from the complex drying dynamics of multicomponent precursor inks, where solvent evaporation and liquid-film convection are coupled, often leading to nonuniform solute migration and morphological defects. Here, we propose a dimethyl sulfoxide/N-methyl-2-pyrrolidone/ethanol (DMSO/NMP/EtOH) ternary co-solvent strategy that synergistically couples precursor coordination chemistry with liquid-film hydrodynamics. NMP weakens the strong DMSO–Pb^{2+} coordination, promoting early nucleation and growth. Meanwhile, EtOH preferentially evaporates to establish a concentration gradient that enhances outward solutal Marangoni flow to counterbalance inward thermal Marangoni flow, enabling uniform solute redistribution across the wet film. This dynamic balance yields perovskite films with enhanced crystallographic orientation, compact coverage, and reduced trap-state densities. Sky-blue PeLEDs achieve a peak EQE of 22.9% at 493 nm with stable electroluminescence, while large-area devices (5 cm^2) maintain 15.8% EQE with uniform emission, representing one of the best results for large-area blue PeLEDs reported. These results extend established co-solvent and flow-control approaches by examining the combined roles of precursor coordination, crystallization kinetics, and wet-film transport in efficient blue PeLEDs with improved area scalability.

Introduction

Metal halide perovskite light-emitting diodes (PeLEDs) have emerged as exceptionally promising candidates for next-generation displays and solid-state lighting, owing to their narrow emission linewidths, high color purity, compositionally tunable bandgaps, and intrinsic compatibility with solution-based manufacturing.[1-6] These attributes render PeLEDs naturally amenable to scalable, high-throughput deposition techniques, including spin coating, blade coating, and roll-to-roll processing.[7-9] However, translating this solution processability into high-performance devices is fundamentally constrained by the complex drying dynamics of precursor inks. Conventional single-solvent systems—typically employing high-polarity aprotic solvents such as dimethyl sulfoxide (DMSO) or N,N-dimethylformamide (DMF)—invariably fail to reconcile the conflicting demands of adequate precursor dissolution, controlled solvent removal, and precise regulation of nucleation and crystal growth.[10,11]

To circumvent these inherent trade-offs, multicomponent solvent engineering has emerged as a powerful strategy to broaden the processing window by introducing solvent constituents with differentiated polarities, coordination abilities, boiling points, and saturated vapor pressures.[12-14] Importantly, unlike conventional antisolvent processing—which relies on instantaneous external perturbation and poses significant challenges for continuous manufacturing[15-17]—multicomponent solvent systems offer intrinsic compatibility with reproducible, large-area fabrication protocols.[18-20] Nevertheless, the mechanistic understanding of how these mixed solvents operate across the entire film-formation cascade remains incomplete, limiting their full potential.

To date, the function of mixed solvents has been predominantly interpreted through the lens of microscopic coordination chemistry. It is well established that solvent molecules interact with Pb^{2+} centers with varying strengths, dictated by their Gutmann donor numbers, Lewis basicity, and steric characteristics, thereby governing precursor solvation structures, intermediate-phase composition, and nucleation/crystallization kinetics. For instance, Xie and co-workers demonstrated that

blending 2-methoxyethanol with propylene carbonate effectively suppresses detrimental low-dimensional phases, enabling high-quality formamidinium-based quasi-2D perovskite films.[21] Similarly, Gallant et al. employed a highly volatile 2-methyltetrahydrofuran/butylamine system to induce a 2D precursor phase, which minimized residual solvent retention and markedly improved the operational stability of α-$FAPbI_3$ devices.[22] These pioneering studies underscore the pivotal role of competitive coordination and solvation engineering in optimizing perovskite crystallization pathways.

Related studies, including our previous work on a DMSO/2-methoxyethanol co-solvent with flash evaporation, have demonstrated that solvent coordination and evaporation kinetics can be regulated to accelerate solvent removal and promote nucleation.[23] However, for pure-bromide quasi-2D blue-emitting films, how to couple coordination-regulated crystallization with spatial solute redistribution during drying to achieve large-area uniformity remains a critical challenge. Furthermore, during wet-film drying, multicomponent solvent systems not only modify the microscopic coordination environment of precursors but also reshape the macroscopic hydrodynamic behavior of the liquid film. Compared with precursor coordination regulation, the roles of solvent-evaporation-induced liquid-film flow and solute migration, as well as their coupled effects on large-area film uniformity, remain less well understood. Solvent evaporation coupled with substrate heating generates temperature and concentration gradients, which induce spatial variations in surface tension and drive Marangoni convection and capillary flows.[24,25] When these internal flows become unbalanced—a common scenario in high-boiling-point solvent systems such as DMSO or DMSO/NMP—precursor solutes undergo nonuniform redistribution toward the central region, leading to local enrichment, spatially heterogeneous crystallization, and morphological defects including pinholes and voids—issues that become particularly acute in large-area coatings.[26-28] Several studies have attempted to regulate drying kinetics via surfactants or low-boiling-point additives,[29,30] yet a unified strategy that simultaneously addresses coordination chemistry and liquid-film

hydrodynamics remains conspicuously absent.

Benefiting from this synergistic "coordination regulation–flow balancing" effect, the sky-blue PeLEDs prepared from the DMSO/NMP/EtOH system achieved a peak external quantum efficiency (EQE) of 22.9% with an effective area of 0.1 cm^2. The devices also showed stable electroluminescence at around 493 nm. Furthermore, large-area PeLEDs with an active area of 5 cm^2 fabricated using the same strategy still achieved an EQE of 15.8% and uniform emission. This confirms the scalable potential of the flow-balanced co-solvent strategy for large-area uniform blue PeLEDs fabrication. This work reveals the synergistic relationship between coordination chemistry and liquid-film hydrodynamics in multicomponent solvent systems. It provides new insights into solvent-engineering design for efficient and scalable perovskite light-emitting devices.

Results

Solvent design for coordination and flow-field regulation

The solvent system governs not only precursor solubility but also nucleation and crystal growth through coordination strength, evaporation rate, and liquid-film flow behavior. In the neat DMSO system (**Figure 1a**), the strong Lewis acid–base interaction between DMSO and Pb^{2+} promotes the formation of $PbBr_2$–DMSO solvated complexes, ensuring sufficient precursor dissolution. However, this overly strong coordination stabilizes the solvated intermediate phase, delaying solvent removal and supersaturation buildup during annealing,[31] which results in retarded nucleation and low nucleation density. Moreover, the release of residual DMSO during subsequent thermal treatment can induce local crystallization inhomogeneity and void-like defects (**Figure S1**). To modulate the coordination strength and improve film morphology, we introduced NMP as a second solvent. NMP exhibits weaker coordination ability toward Pb^{2+} than DMSO, moderately weakening the DMSO-dominated strong coordination environment and facilitating the transformation of solvated intermediates into the perovskite crystalline phase. Meanwhile, its lower saturated vapor pressure and higher

boiling point (**Table S1**) provide a broader kinetic window for crystal growth during desolvation. Consequently, the DMSO/NMP binary system displays more favorable crystallization regulation: earlier nucleation is promoted while the extended solvent evaporation period facilitates further grain growth (**Figure 1b**).

However, regulation based solely on microscopic coordination and evaporation kinetics cannot fully ensure spatial uniformity at the macroscopic film scale. During wet-film drying, solvent evaporation coupled with substrate heating generates temperature and concentration gradients across the liquid film, driving Marangoni convection and capillary compensation flows. The surface-tension gradient within the liquid film can be expressed as:

$$\nabla_S \gamma = \frac{\partial \gamma}{\partial T} \nabla_S T + \frac{\partial \gamma}{\partial C} \nabla_S C \quad (1)$$

where γ is the surface tension of the liquid film, T is the temperature, C is the concentration and ∇_S is the gradient operator along the liquid–gas interface.[32] The first and second terms on the right-hand side represent the surface-tension gradients arising from temperature (thermal Marangoni) and concentration (solutal Marangoni) gradients, respectively. The balance between these opposing Marangoni flows plays an important role in regulating the spatial redistribution of precursor solutes and the resulting film uniformity.

In the neat DMSO and DMSO/NMP systems (Figure 1a,b), the high boiling points and low volatility of both DMSO and NMP make it difficult to establish a pronounced compositional concentration gradient during the early drying stage. Consequently, the outward solutal Marangoni driving force induced by the concentration gradient is relatively weak and cannot effectively counterbalance the inward thermal Marangoni flow dominated by the temperature gradient.[33] This flow imbalance drives precursor solutes to continuously migrate toward the center of the liquid film, eventually leading to solute enrichment in the central region. Notably, this effect becomes more pronounced after introducing NMP: the overall evaporation rate is further reduced and

the flowable lifetime of the liquid film is prolonged, exacerbating the inward Marangoni-dominated solute accumulation. Thus, while the DMSO/NMP binary system promotes earlier nucleation and more sufficient crystal growth at the microscopic coordination level, it aggravates nonuniform solute migration toward the central region at the macroscopic scale.

Based on the above analysis, we further introduced EtOH as a third solvent component to regulate Marangoni convection in the liquid film. Owing to its low boiling point, high volatility, and low surface tension, EtOH preferentially evaporates during the early annealing stage, establishing a pronounced compositional concentration gradient within the liquid film that significantly enhances the outward solutal Marangoni flow (**Figure 1c**). This outward flow effectively counterbalances the inward thermal Marangoni flow, promoting a dynamic equilibrium of the internal flow field. Meanwhile, the high volatility of EtOH accelerates the buildup of supersaturation and facilitates earlier nucleation. Benefiting from the regulated solute transport, precursor species are redistributed more uniformly across the entire wet film, yielding high-quality perovskite films with homogeneous crystallization, compact coverage, and reduced defect density (Figure S1).

To further validate the proposed mechanism, we performed coupled simulations of temperature field, concentration field, and internal fluid behavior during droplet drying using COMSOL Multiphysics. During annealing, substrate heating combined with evaporative cooling at the free surface establishes a pronounced temperature gradient within the liquid film: regions near the substrate and droplet edge maintain relatively higher temperatures, while the top and central regions are more strongly affected by evaporative cooling and thus exhibit lower temperatures (**Figure S2**). Since surface tension generally decreases with increasing temperature, this nonuniform temperature distribution generates a thermal Marangoni driving force directed from the edge toward the center. Regarding the concentration field (**Figure 1d–f**), the high-boiling-point solvents in the neat DMSO and DMSO/NMP systems fail to establish a significant compositional gradient during the early drying stage, resulting in a weak

outward solutal Marangoni driving force. In contrast, in the DMSO/NMP/EtOH ternary system, the preferential evaporation of EtOH significantly accelerates solvent removal and establishes a more pronounced compositional concentration gradient, enhancing the outward solutal Marangoni driving force. The combined effects of the temperature and concentration fields ultimately determine the flow-field direction (**Figure 1g–i**). In the neat DMSO and DMSO/NMP systems, the outward solutal driving force is insufficient to counteract the inward thermal driving force, and the internal flow is dominated by inward Marangoni flow toward the center, driving continuous solute migration and central enrichment—an effect exacerbated by the prolonged liquid-film lifetime in the DMSO/NMP system. In the ternary system, however, the EtOH-enhanced outward driving force partially counterbalances the inward thermal driving force, converting the streamlines from inward to low-velocity outward flow. This suppresses continuous solute migration toward the center and promotes more uniform solute redistribution.

Collectively, the COMSOL simulation results suggest that the DMSO/NMP/EtOH ternary solvent system improves film formation not only by accelerating solvent evaporation but also by regulating temperature and concentration gradients and the resulting Marangoni convection. In particular, the enhanced solutal Marangoni driving force partially counterbalances the opposing thermal contribution, thereby reducing local solute enrichment and creating more favorable conditions for uniform nucleation and controlled crystal growth. To assess the relevance of the proposed flow-balancing mechanism to spin-coated film formation, we interrupted spin coating after 20 s and examined samples prepared using DMSO, DMSO/NMP, and DMSO/NMP/EtOH by macroscopic photography and subsequent optical microscopy (**Figure S3**). For each solvent system, two different edge regions of the same sample were examined to assess the spatial distribution of edge deposition. When considered alongside the simulated flow fields, the observed differences in edge-deposition patterns provide qualitative, indirect support for a possible hydrodynamic contribution to precursor redistribution during film formation.

Precursor Solution Chemistry and Nucleation Kinetics

To validate the above simulation findings and elucidate the solution chemistry and film formation kinetics, we systematically characterized the precursor solutions and the resulting perovskite films. The size distribution of colloidal species in precursor solutions exerts a profound influence on subsequent nucleation behavior. Dynamic light scattering (DLS, **Figure 2a–c**) reveals that the neat DMSO system exhibits a colloidal size of approximately 1 nm, indicating that the precursors predominantly exist as small solvated complexes. Upon introduction of NMP, the colloidal size increases to approximately 100 nm, suggesting that NMP induces pronounced precursor pre-aggregation. Further addition of EtOH increases the size to approximately 147 nm. This trend is consistent with the distinct dissolution capabilities of different solvent systems toward $PbBr_2$ (**Figure S4**): $PbBr_2$ is completely dissolved in neat DMSO, whereas solution turbidity gradually increases with increasing NMP content. The Gutmann donor numbers of DMSO and NMP are 29.8 and 27.3 kcal mol^{-1}, respectively. DMSO, possessing stronger Lewis basicity, more readily forms stable $PbBr_2$–DMSO solvated complexes with Pb^{2+}, thereby enhancing $PbBr_2$ solubility.[34] The relatively weaker coordination ability of NMP partially weakens the DMSO-dominated solvation environment, driving the precursor species from a highly dissolved state toward a moderately pre-aggregated state. The further addition of EtOH, with its much weaker polarity and coordination ability, further reduces the solvation capability of the system and promotes continued colloidal growth.

Fourier transform infrared (FTIR) spectroscopy (**Figure 2d,e** and **Figure S5**) further elucidates the influence of different solvent components on the precursor coordination environment. In the neat DMSO system, the S=O stretching vibration peak of DMSO shifts from 1042 cm^{-1} to 1046 cm^{-1} upon addition of perovskite precursors, indicating pronounced coordination interaction between DMSO and Pb^{2+}. Upon introduction of NMP, the S=O peak of neat DMSO shifts from 1042 cm^{-1} to 1044 cm^{-1}, suggesting that NMP alters the local solvation environment of DMSO; after precursor addition, this peak further shifts only slightly to 1045 cm^{-1}, indicating that the interaction between

DMSO and perovskite precursors is significantly weakened. In contrast, the S=O peak position in the DMSO/EtOH system remains almost unchanged, suggesting a relatively weak direct interaction between EtOH and DMSO. To further verify the coordination interactions between DMSO/NMP and $PbBr_2$, $PbBr_2$ needle-like crystals were grown in DMSO and NMP solvents, respectively, followed by XRD characterization (**Figure S6**). The diffraction peaks of both solvated samples are distinctly different from those of pristine $PbBr_2$ powder, confirming that both solvents can coordinate with $PbBr_2$ to form solvated intermediate phases with characteristic crystal structures, rather than simply inducing $PbBr_2$ recrystallization.[35] Notably, the NMP–$PbBr_2$ sample exhibits multiple characteristic diffraction peaks distinct from those of DMSO–$PbBr_2$, further confirming that NMP can participate in the solvation and coordination process of Pb^{2+} and induce the formation of an intermediate-phase structure different from that of DMSO–$PbBr_2$.

Based on the above solubility, DLS, FTIR, and XRD results, we constructed a LaMer-type concentration–time schematic (**Figure 2f**) to describe the kinetic differences in the transition of precursors from the solution state to the crystalline state under different solvent systems. In the neat DMSO system, the strong DMSO–Pb^{2+} coordination overly stabilizes the precursors, leading to a slow increase in the effective precursor concentration and delayed entry into the nucleation zone, resulting in low nucleation density. Upon introduction of NMP, the DMSO-dominated strong coordination environment is weakened, reducing the resistance for precursors to transform from stable complexed species to nucleation-active species, allowing the system to enter the nucleation zone earlier. Meanwhile, the low evaporation rate of NMP significantly broadens the subsequent crystal-growth window, manifesting as a binary crystallization feature of "early nucleation–slow growth." Further addition of EtOH increases the overall evaporation rate of the solvent system, enabling the liquid film to reach supersaturation more rapidly and further promoting high-density nucleation,[36,37] simultaneously, the flow-field balancing effect induced by EtOH evaporation suppresses local solute enrichment and enables a more uniform spatial distribution of nuclei.

The distinct nucleation processes are directly visualized by in situ optical microscopy (**Figure 2g**). After dropping equal volumes of precursor solutions onto the same glass substrate, only a small number of nuclei appear in the neat DMSO system after 3 min; the number of nuclei increases markedly in the DMSO/NMP system; and the DMSO/NMP/EtOH system exhibits the highest nucleation density with the most uniform spatial distribution upon completion of nucleation. In addition to the changes in precursor solvation, the wetting properties of the mixed-solvent systems may also contribute to the observed differences in early-stage crystallization. To examine this contribution, contact angle, surface tension, and rheological measurements were performed. Contact angle (**Figure S7**) and surface tension (**Figure S8**) measurements yield apparent spreading coefficients for the DMSO, DMSO/NMP, and DMSO/NMP/EtOH systems, calculated using the following equation:

$$S = \gamma_{LG}(cos\,\theta - 1) \tag{2}$$

where S is the apparent spreading coefficient, γ_{LG} is the liquid–gas interfacial surface tension, and θ is the contact angle of the precursor solution on the substrate.[38,39] A value of S closer to zero indicates better wetting and spreading ability. The calculated S values for the three systems are -5.82, -2.70, and -0.61 mN m^{-1}, respectively. The ternary system exhibits an S value closest to zero, indicating the best wetting and spreading ability, which favors the formation of a continuous and uniform precursor wet film and suppresses dewetting and local shrinkage during annealing. According to the heterogeneous nucleation model:

$$\Delta G_{\mathrm{het}} = \Delta G_{\mathrm{hom}} \frac{(2 + cos\,\theta)(1 - cos\,\theta)^2}{4} \tag{3}$$

where ΔGhet is the free-energy barrier for heterogeneous nucleation, ΔGhom is the free-energy barrier for homogeneous nucleation, and θ is the contact angle of the precursor solution on the substrate.[40,41] This expression indicates that a reduction in

contact angle lowers the free-energy barrier for heterogeneous nucleation. In addition, rheological measurements (**Figure S9**) show that the ternary system exhibits the lowest apparent viscosity, facilitating liquid-film spreading and rapid solute redistribution in response to the concentration gradient established by EtOH evaporation. Atomic force microscopy (AFM, **Figure S10**) further reveals that surface roughness decreases progressively upon sequential introduction of NMP and EtOH, with the ternary system yielding the smoothest and most compact film morphology, consistent with the above nucleation and crystallization kinetics.

To elucidate the film formation mechanism throughout the entire fabrication process, we monitored the time-dependent absorbance using in situ UV–vis spectroscopy across both the spin-coating and subsequent annealing stages. During spin coating, the absorbance at 430 nm begins to increase earliest in the DMSO/NMP/EtOH system, followed by DMSO/NMP and neat DMSO, with the ternary system exhibiting the most pronounced and sustained signal buildup (**Figure S11**). Together with the coordination and optical microscopy results, this confirms an earlier onset of nucleation in the mixed-solvent systems. Following spin coating, the in situ absorption spectra during annealing (**Figure 2h–j**) reveal that all films gradually develop distinct absorption bands in the 420–480 nm region, indicating the progressive formation of the quasi-2D bromide perovskite crystalline phase. Notably, the maximum absorption intensity is observed at approximately 430 nm (**Figure S12**). Tracking the time evolution of the absorbance at this 430 nm peak reveals that the neat DMSO system reaches its maximum intensity at approximately 140.7 s, whereas the DMSO/NMP and DMSO/NMP/EtOH systems peak at approximately 171.6 s and 168.6 s, respectively. The prolonged formation of crystalline-phase absorption in the latter two systems suggests that the low saturated vapor pressure and slow evaporation of NMP broaden the crystal-growth window, enabling a slower and more controllable formation process of the perovskite crystalline phase.[42] Compared with the DMSO/NMP system, the ternary system reaches the maximum absorption intensity slightly earlier, which can be attributed to the rapid evaporation of EtOH and the moderately increased overall solvent removal rate.

Photophysical Properties and Structural Characteristics of Perovskite Films

The UV–vis absorption spectra of perovskite films prepared from different solvent systems are shown in **Figure 3a**. The film prepared from the neat DMSO system exhibits the lowest absorption intensity, mainly attributable to void defects and discontinuous coverage that reduce the effective light-absorbing area and crystalline-phase continuity. The DMSO/NMP system shows enhanced absorption intensity, indicating that NMP improves film coverage and crystallization quality. The DMSO/NMP/EtOH system exhibits the highest absorption intensity, confirming that the ternary co-solvent strategy promotes the uniform distribution of crystals and the formation of a dense, continuous, high-quality perovskite film.[43]

Steady-state photoluminescence (PL) spectra (**Figure 3b**) show that the neat DMSO system exhibits the lowest PL intensity, indicating a high density of defect states that induce trap-assisted nonradiative recombination. Upon sequential introduction of NMP and EtOH, the PL peak intensity is significantly enhanced, indicating effective suppression of nonradiative recombination and markedly improved emissive-layer quality.[44] Photoluminescence quantum yield (PLQY) measurements (**Figure S13**) further confirm that the ternary system exhibits the highest PLQY, corresponding to the lowest nonradiative recombination loss. Time-resolved photoluminescence (TRPL, **Figure 3c** and **Table S2**) reveals average carrier lifetimes of 2.27 ns, 3.35 ns, and 4.16 ns for the DMSO, DMSO/NMP, and DMSO/NMP/EtOH systems, respectively. The prolonged carrier lifetime indicates that defect-assisted nonradiative recombination pathways are effectively reduced.[45]

Temperature-dependent PL measurements (**Figure 3d–f** and **Figure S14**) were performed to evaluate the exciton thermal stability of the perovskite films. The integrated PL intensities at different temperatures were fitted using the Arrhenius model:

$$I(T) = \frac{I_0}{1 + A\,exp\left[-\frac{E_b}{(k_B T)}\right]} \tag{4}$$

where $I(T)$ is the integrated PL intensity at temperature T, I_0 is the integrated PL intensity in the low-temperature limit, A is a constant related to the thermally activated nonradiative process, E_b is the apparent exciton binding energy, and k_B is the Boltzmann constant.[46] A larger E_b indicates higher exciton stability against thermal perturbation. The neat DMSO system exhibits the most pronounced PL thermal quenching and a relatively low apparent exciton binding energy (65.56 meV), attributable to residual solvent and defects such as buried-interface voids that introduce nonradiative recombination centers. Upon introduction of NMP, the DMSO-dominated strong coordination environment is partially weakened and the crystallization process becomes more controllable, reducing defects and improving exciton thermal stability (E_b=86.23 meV). The DMSO/NMP/EtOH ternary system simultaneously optimizes the precursor coordination state and the liquid-film flow-field distribution, resulting in more uniform crystallization, more compact film coverage, and lower defect-assisted nonradiative recombination losses. Consequently, its integrated PL intensity decreases most slowly with increasing temperature and exhibits the highest apparent exciton binding energy.[47,48] Space-charge-limited current (SCLC) measurements **(Figure S15, S16**) reveal trap-state densities of 2.07×10^{17}, 1.96×10^{17}, and 1.49×10^{17} cm^{-3} for the DMSO, DMSO/NMP, and DMSO/NMP/EtOH systems, respectively. The progressively decreasing trap-state density further confirms that the mixed-solvent strategy effectively reduces bulk and interfacial defects in the films.

Grazing-incidence wide-angle X-ray scattering (GIWAXS, **Figure 3g–i**) reveals the influence of different solvent systems on the crystallization behavior of the perovskite films. Under the same intensity scale, the main scattering signals of the three samples appear at similar positions, confirming that solvent-system regulation does not change the primary crystalline phase. Compared with the neat DMSO system, the DMSO/NMP system shows an enhanced (100) scattering signal, indicating that NMP improves the crystallographic ordering of the perovskite film. After further introduction of EtOH, the DMSO/NMP/EtOH system exhibits a brighter and more concentrated (100) scattering feature, suggesting that the ternary solvent system further promotes ordered crystal

growth. X-ray diffraction (XRD, **Figure S17**) complements the GIWAXS findings: all three films exhibit distinct diffraction peaks at around 15.5° and 30.8°, corresponding to the (100) and (200) planes of the cubic perovskite phase, respectively. The DMSO/NMP and DMSO/NMP/EtOH systems show markedly enhanced diffraction peak intensities compared with the neat DMSO system, with the ternary system exhibiting the strongest (200) diffraction peak. Azimuthal integrated intensity analysis (**Figure S18**) shows that all three samples reach their maxima at around 90°, indicating a certain degree of preferred orientation. As the solvent system evolves from neat DMSO to DMSO/NMP and DMSO/NMP/EtOH, the azimuthal integrated intensity of the (100) plane gradually increases, with the ternary system exhibiting the highest peak intensity, suggesting a more concentrated (100) orientation and the best crystallographic ordering.[49]

The above XRD and GIWAXS results are highly consistent with the in situ crystallization kinetics, film morphology, and photophysical characterization discussed above. They further demonstrate that the DMSO/NMP/EtOH ternary solvent system can effectively optimize the nucleation and crystal-growth processes without changing the main crystalline phase of the perovskite, yielding high-quality perovskite films with more uniform crystallization, improved orientation, and fewer defects.

Fabrication and Characterization of Perovskite Light-Emitting Diodes

To evaluate the influence of different solvent systems on PeLED performance, devices with an indium tin oxide (ITO)/ poly(3,4-ethylenedioxythiophene): poly(styrenesulfonate) (PEDOT:PSS)/perovskite/TPBi/LiF/Al structure were fabricated, as illustrated in **Figure 4a**. The current density–voltage–luminance (*J*-*V*-*L*) characteristics shown in **Figure 4b** reveal that, with increasing driving voltage, the current density of all devices gradually increases while the luminance first rises and then falls; among them, the device based on the DMSO/NMP/EtOH ternary system exhibits the highest luminance output. **Figure 4c** shows the EQE–current density curves (EQE-*J*) of devices prepared from different solvent systems, and the corresponding EQE–luminance curves are shown in **Figure S19**. The device based on the pure DMSO

system exhibits a peak EQE of 16.9%. Upon introduction of NMP, the peak EQE increases to 20.0%, indicating that NMP-mediated regulation of coordination and nucleation kinetics effectively improves the crystallization quality of the emissive layer. Further addition of EtOH yields the best-performing device, with a peak EQE of 22.9%. This enhancement is primarily attributed to the EtOH-induced regulation of the Marangoni flow field during wet-film drying, which enables more uniform redistribution of precursor solutes, resulting in an emissive layer with more homogeneous crystallization, more compact coverage, and fewer defects—consistent with the in situ crystallization, GIWAXS, temperature-dependent PL, and SCLC results discussed above.

To further verify the necessity of this coordination–hydrodynamic synergy, we fabricated control devices using a DMSO/EtOH binary system. As shown in **Figure S20**, the DMSO/EtOH-based device exhibits a peak EQE of only 14.1%, which is even lower than that of the neat DMSO device (16.9%) and significantly inferior to the NMP-containing counterparts. This result strongly suggests that without NMP-mediated coordination regulation to broaden the crystallization window, the EtOH-driven rapid evaporation and flow changes lead to excessively fast supersaturation and poor crystal growth, thereby failing to deliver high efficiency. This comparison directly corroborates the proposed complementary roles of NMP and EtOH: NMP tailors the crystallization kinetics to a suitable window, while EtOH ensures uniform solute distribution within that window. Finally, the statistical distribution of EQE for ten independent devices (**Figure 4d**) shows that the ternary-system devices exhibit a high average EQE with a narrow performance distribution, confirming the good reproducibility and process reliability of this strategy.

We further examined the spectral and operational stability of the devices. The electroluminescence (EL) spectra measured under different driving voltages (3.5–7.0 V, **Figure 4e**) show that the EL peak of the ternary-system device remains stable at around 493 nm without detectable peak shift (the voltage-dependent EL spectra of the neat DMSO and DMSO/NMP based devices are shown in **Figure S21**), indicating that the

emissive layer prepared from the ternary system exhibits good phase-composition and spectral stability.[50] Regarding operational stability, the T_{50} values for the DMSO, DMSO/NMP, and DMSO/NMP/EtOH systems are 163, 344, and 821 s, respectively (**Figure S22**), with the ternary-system device showing the best operational stability. This improvement is attributed to the uniform crystallization, compact coverage, and lower trap-state density, which effectively suppress trap-assisted recombination and local electric-field concentration, thereby retarding device degradation during operation. The ternary-system device achieves stable sky-blue electroluminescence at around 493 nm, with Commission Internationale de l'Eclairage (CIE) coordinates of (0.059, 0.336) (**Figure 4f**).

To further verify the applicability of the ternary solvent system for large-area device fabrication, PeLEDs with an active area of 5 cm^2 were fabricated. **Figure 4g,h** present the *J-V-L* characteristics and the corresponding EQE-*J* curve of the large-area device (inset: photograph of the operating device; digital photographs are shown in **Figure S23**), which achieves a peak EQE of 15.8%, corresponding to a performance decay of only approximately 31% relative to the small-area device, demonstrating that high efficiency can be maintained upon device-area scaling. Uniform and continuous sky-blue emission is observed across the entire active region, free from dark regions or localized bright spots, confirming that the ternary system effectively supports the formation of a uniform large-area emissive layer. In large-area film formation, solvent-evaporation-induced Marangoni flow often exacerbates nonuniform solute redistribution, whereas the ternary system, by balancing opposing Marangoni flows, effectively suppresses spatial solute enrichment and localized crystallization inhomogeneity, thereby ensuring emission uniformity of the large-area devices. As summarized in **Figure 4i** and **Table S4**, the large-area blue PeLEDs fabricated in this work rank among the best-reported efficiencies for large-area (≥1 cm^2) blue PeLEDs to date. Collectively, these results establish that the DMSO/NMP/EtOH ternary solvent system is not only suitable for high-efficiency small-area PeLEDs but also provides a viable route toward scalable large-area perovskite light-emitting devices.

Discussion

In this work, we developed a DMSO/NMP/EtOH ternary co-solvent strategy for efficient and scalable pure-bromide quasi-2D sky-blue PeLEDs. Building on previous co-solvent approaches that primarily focused on accelerating solvent removal and nucleation, the present study further examines the relationship between precursor coordination, crystallization kinetics, and liquid-film transport. NMP modifies the DMSO-dominated solvation environment, promoting earlier nucleation while extending the subsequent crystallization period. Meanwhile, EtOH regulates evaporation kinetics, wetting properties, and surface-tension gradients. The COMSOL simulations suggest that the enhanced solutal Marangoni driving force partially counterbalances the inward thermal contribution, providing a possible explanation for the improved spatial redistribution of precursor solutes.

The combined regulation yields perovskite films with improved crystallographic ordering, compact coverage, and reduced trap-state density. The resulting sky-blue PeLEDs achieve a peak EQE of 22.9% at 493 nm and maintain an EQE of 15.81% over an active area of 5 cm^2 with uniform emission. These findings extend the understanding of co-solvent-assisted film formation by highlighting the combined roles of precursor solvation, crystallization kinetics, and liquid-film transport in area-scalable sky-blue PeLED fabrication.

Materials and methods

Materials

N-Methyl-2-pyrrolidone (NMP), Molybdenum oxide (MoO_x) and ethanolamine (ETA) were procured from Sigma-Aldrich. Indium Tin Oxide and lead (II) bromide ($PbBr_2$) were supplied by Liaoning Preferred New Energy Technology Company. 2-Bromoethylamine hydrobromide (BEABr) were provided by Aladdin. Phenethylammonium bromide (PEABr) and 1,3,5-Tris(1-phenyl-1H-benzimidazol-2-yl) benzene (TPBi) were purchased from Xi'an Yuri Solar Co. Cesium bromide (CsBr) was purchased from Liaoning Youxuan New Energy Co. Ltd. poly(3,4-ethylenedioxythiophene): poly(styrenesulfonate) (PEDOT: PSS, Clevios Al 4083) was

purchased from Heraeus. All chemicals were used as received without additional purification.

Precursor Solution fabrication

The DMSO/NMP/EtOH perovskite precursor solution preparation: PEABr, CsBr, $PbBr_2$ and BEABr at a molar ratio of 0.8: 1.2: 1: 0.15 (the concentration of $PbBr_2$ was 0.15 M) were dissolved in DMSO/NMP/EtOH mixed solvent (The volume ratio: DMSO: NMP: EtOH= 4: 1: 0.25). The DMSO/NMP perovskite precursor solution preparation: PEABr, CsBr, $PbBr_2$ and BEABr at a molar ratio of 0.8: 1.2: 1: 0.15 (the concentration of $PbBr_2$ was 0.15 M) were dissolved in DMSO/NMP mixed solvent (The volume ratio: DMSO: NMP = 4:1). The DMSO perovskite precursor solution preparation: PEABr, CsBr, $PbBr_2$ and BEABr at a molar ratio of 0.8:1.2:1:0.15 (the concentration of $PbBr_2$ was 0.15 M) were dissolved in pure DMSO solvent. All solvents were used directly as received without any further treatment or purification.

Device fabrication

Patterned ITO glass substrates were sequentially ultrasonically cleaned in acetone, ethanol, and deionized water for 20 min each before use, followed by UV–ozone treatment for 30 min. ETA was first dissolved in ethanol at a volume ratio of 4: 20. A certain amount of this solution was then added to 1 mL of PEDOT:PSS to prepare the ETA-PEDOT mixed solution, with the ETA volume fraction controlled at 0.4%. Before use, the ETA-PEDOT solution was filtered through a 0.22 μm aqueous syringe filter to remove large particles and insoluble residues. In ambient air, the modified ETA-PEDOT solution was dropped onto the UV-ozone-treated ITO electrode and spin-coated at 2500 rpm for 40 s to form the hole transport layer (HTL). The substrate was then annealed on a hot plate at 140 °C for 15 min. Subsequently, the substrate was transferred into a nitrogen-filled glovebox for perovskite film deposition. A 100 μL quasi-2D perovskite precursor solution was dropped onto the center of the substrate and spin-coated at 4500 rpm for 60 s to obtain the perovskite film. The sample was then heated at 70 °C for 10 min to improve crystallization. Subsequently, TPBi (40 nm), LiF (1 nm), and Al (120 nm) layers were sequentially deposited using a thermal evaporation

system under a vacuum of 1.0×10^{-4}Pa. The effective area of the PeLEDs was defined by the overlap between the patterned ITO and Al electrodes and was 0.10 cm^2. For large-area PeLEDs, 1000 μL of quasi-2D perovskite precursor solution was dropped onto the center of the substrate and spin-coated at 4000 rpm for 60 s to form the perovskite layer. The other functional layers were fabricated following the same procedures described above. The active area of the large-area PeLEDs, defined by the overlap between the patterned ITO and Al electrodes, was 5 cm^2.

Characterization

The morphology and microstructure of perovskite films deposited on ITO substrates were investigated using SEM (Hitachi 4800). X-ray diffraction (XRD) measurements of the 2D perovskites were performed using a D8 Advance diffractometer equipped with a conventional Cu-target X-ray tube (Cu K-alpha, $\lambda = 1.5405$ Å). Fourier transform infrared (FTIR) spectra were recorded using a Nicolet iS50 FTIR spectrometer in the range 4000 cm^{-1}~400 cm^{-1}. PLQY and TRPL measurements were performed on perovskite films deposited on quartz substrates using an Edinburgh FLS920 fluorescence spectrometer under 365 nm excitation. The surface morphology of the samples was characterized using a Bruker Multimode 8 system AFM in non-contact mode. UV–vis absorption spectra of the samples were measured using a Shimadzu UV-3101PC spectrophotometer over the wavelength range of 400–800 nm. GIWAXS measurements were performed at 1W1A Diffuse X-ray Scattering Station of the Beijing Synchrotron Radiation Facility (BSRF-1W1A). PL spectra were measured using a Hitachi F-7000 fluorescence spectrophotometer. The J-V characteristics and luminance-voltage curves of the devices were measured using a Keithley 2612 source meter coupled with a Konica Minolta LS-110 luminance meter. EL spectra were collected using a fiber-optic spectrometer. The EQE was calculated based on the Lambertian emission model using the measured luminance, current, and electroluminescence spectra. All other measurements were performed on the Test Go scientific research service platform.

Simulation of Marangoni-Driven Solvent Flow

COMSOL Multiphysics was used to perform finite-element simulations of the heat transfer and fluid behavior of three mixed solvent systems based on DMSO, DMSO/NMP, and DMSO/NMP/EtOH. By constructing a multiphysics coupled model involving the concentration field, the internal vortex structures within the droplets could be simulated.

Governing equations: In the numerical simulation, the precursor liquid film was treated as a continuum. The evolution of mass, momentum, and energy in the fluid was described using the transport theorem, which relates the temporal change of a physical quantity in a control volume to its accumulation and net flux across the control surface. The corresponding general transport equation is expressed as follows:

$$\frac{dN}{dt} = \int_V \eta\rho dV + \oint_S \eta\rho\vec{u}dS \tag{5}$$

where N is the total physical quantity in the system, η is the corresponding quantity per unit mass, ρ is the fluid density, V is the control volume, S is the control surface, u is the velocity vector, Different conservation equations can be obtained by assigning different values to η, such as η=1 for mass conservation, η=u for momentum conservation, and energy conservation.

$$\frac{\partial\rho}{\partial t} + \nabla \bullet (\rho u) = 0 \tag{6}$$

$$\nabla \bullet u = 0 \tag{7}$$

The mass conservation equation, also known as the continuity equation, describes the relationship between fluid motion and mass distribution. It indicates that the temporal variation of fluid mass within a control volume is balanced by the net mass flux across the control surface, as expressed in Equation (6). For an incompressible fluid, the density remains constant, and the continuity equation can be simplified to Equation (7).

$$\frac{\partial(\rho u)}{\partial t} + \nabla \bullet (\rho uu) = \nabla \bullet [\mu(\nabla u + \nabla u^T)] - \nabla p + F \tag{8}$$

where p is the fluid pressure, μ is the viscosity, and F is the body force. The momentum conservation equation, also known as the Navier–Stokes (N-S) equation, describes the fundamental mechanical laws governing viscous fluid flow. As expressed in Equation (8), it indicates that the rate of momentum increase within a control volume

is equal to the sum of the external forces acting on it per unit time. Similarly, for an incompressible fluid, the fluid density and viscosity are assumed to be constant. The energy equation describes the relationship between the temperature field and other physical parameters of the moving fluid. It is based on the law of energy conservation and Fourier's law of heat conduction, and can be expressed as follows:

$$\frac{\partial(\rho C_p T)}{\partial t} + \nabla \bullet \left(\rho C_p u T\right) = \nabla \bullet [\nabla(kT)] + Q \quad (9)$$

where C_p is the specific heat capacity, T is the temperature, k is the thermal conductivity, and Q is the heat source term.

Data availability

The data that support the findings of this study are available from the corresponding author upon reasonable request.

Acknowledgements

This work was supported by the National Natural Science Foundation of China Nos. 62175235, 62525405, and the Jilin Province Science and Technology Research Project of 20260201032GX.

Author information

Author notes

These authors contributed equally: Longxiang Yang, Kai Sun.

Authors and Affiliations

State Key Laboratory of Luminescence Science and Technology, Changchun Institute of Optics, Fine Mechanics and Physics, Chinese Academy of Sciences, Changchun 130033, P. R. China

Longxiang Yang, Xiaoyang Guo, Ying Lv, Tienan Wang & Xingyuan Liu

University of Chinese Academy of Sciences, Beijing 100049, P. R. China

Longxiang Yang

State Key Laboratory of Polymer Science and Technology, Changchun Institute of Applied Chemistry, Chinese Academy of Sciences, Changchun 130022, P. R. China

Jiang Wu

Institute for Advanced Materials & Guangdong Provincial Key Laboratory of Optical

Information Materials and Technology, South China Academy of Advanced Optoelectronics, South China Normal University, Guangzhou 510006, China

Kai Sun

Beijing Institute of Technology, Beijing 100081, P. R. China

Yafang Ren

National Engineering Research Center for Diffraction Gratings Manufacturing and Application, Changchun Institute of Optics, Fine Mechanics and Physics, Chinese Academy of Sciences, Changchun 130033, P. R. China

Bayanheshig

Contributions

X.G., J.W. and X.L. conceived and supervised the project. L.Y. and K.S. fabricated the devices, performed the characterizations and analyzed the data. Y.R., Y.L., T.W. and B. contributed to the material synthesis and experimental measurements. L.Y. wrote the manuscript. All authors discussed the results and commented on the manuscript.

Corresponding authors

Correspondence to Xiaoyang Guo, Jiang Wu or Xingyuan Liu.

References

1 Xing, Z. *et al.* Ions-induced Assembly of Perovskite Nanocomposites for Highly Efficient Light-Emitting Diodes with EQE Exceeding 30%. *Advanced Materials* **36**, 2406706 (2024).

2 Yu, Y. *et al.* Efficient Blue Perovskite LEDs via Bottom-Up Charge Manipulation for Solution-Processed Active-Matrix Displays. *Advanced Materials* **37**, 2503234 (2025).

3 Wei, K. *et al.* Perovskite heteroepitaxy for high-efficiency and stable pure-red LEDs. *Nature* **638**, 949-956 (2025).

4 Liu, N. *et al.* Fluorine-modified passivator for efficient vacuum-deposited pure-red perovskite light-emitting diodes. *Light: Science & Applications* **14**, 118 (2025).

5 Jiang, J. *et al.* Efficient Red Perovskite LEDs with Iodine Management via Volatile Additive I2. *Advanced Materials* **37**, 2503699 (2025).

6 Yang, F. *et al.* Rational adjustment to interfacial interaction with carbonized polymer dots enabling efficient large-area perovskite light-emitting diodes. *Light: Science & Applications* **12**, 119 (2023).

7 Kim, J. S. *et al.* Kinetically-controlled intermediate-direct-pinning for homogeneous energy landscapes in quasi-two-dimensional perovskites for efficient and narrow blue emission. *Nature Communications* **16**, 9590 (2025).

8 Baek, S.-D. *et al.* Tailoring crystallization kinetics for scalable and efficient large-area perovskite light-emitting diodes. *Science Advances* **12**, eaef3336 (2026).

9 Parvazian, E. & Watson, T. The roll-to-roll revolution to tackle the industrial leap for perovskite

solar cells. *Nature Communications* **15**, 3983 (2024).
10 Cho, S.-B., Li, C.-X., Kim, D.-Y. & Park, I.-K. High-Luminance Blue Quasi-2D Perovskite Light-Emitting Diodes by Engineering Polarity-Controlled Solvent-Film Interaction. *Advanced Functional Materials* **n/a**, e76460 (2026).
11 Wang, Y. *et al.* Beyond rapid nucleation: unveiling the role of solvent–precursor interactions in antisolvent-free perovskite fabrication. *Energy & Environmental Science* **19**, 2988-2998 (2026).
12 Huang, X. *et al.* Solvent racing crystallization: Low-solvation dispersion cosolvents for high-quality halide perovskites in photovoltaics. *Joule* **7**, 1556-1573 (2023).
13 Yoo, J. W. *et al.* Efficient perovskite solar mini-modules fabricated via bar-coating using 2-methoxyethanol-based formamidinium lead tri-iodide precursor solution. *Joule* **5**, 2420-2436 (2021).
14 Li, N. *et al.* Liquid medium annealing for fabricating durable perovskite solar cells with improved reproducibility. *Science* **373**, 561-567 (2021).
15 Jeon, N. J. *et al.* Solvent engineering for high-performance inorganic–organic hybrid perovskite solar cells. *Nature Materials* **13**, 897-903 (2014).
16 Huang, H.-H. *et al.* A simple one-step method with wide processing window for high-quality perovskite mini-module fabrication. *Joule* **5**, 958-974 (2021).
17 Yang, M. *et al.* Perovskite ink with wide processing window for scalable high-efficiency solar cells. *Nature Energy* **2**, 17038 (2017).
18 Liu, C., Cheng, Y.-B. & Ge, Z. Understanding of perovskite crystal growth and film formation in scalable deposition processes. *Chemical Society Reviews* **49**, 1653-1687 (2020).
19 Chao, L. *et al.* Solvent Engineering of the Precursor Solution toward Large-Area Production of Perovskite Solar Cells. *Advanced Materials* **33**, 2005410 (2021).
20 Taylor, A. D. *et al.* A general approach to high-efficiency perovskite solar cells by any antisolvent. *Nature Communications* **12**, 1878 (2021).
21 Guo, Y. *et al.* Weakly Coordinated Co-Solvent Strategy Enables Anti-Solvent-Free Fabrication of High-Efficiency Perovskite Light-Emitting Diodes. *Advanced Functional Materials* **36**, e17075 (2026).
22 Gallant, B. M. *et al.* A green solvent enables precursor phase engineering of stable formamidinium lead triiodide perovskite solar cells. *Nature Communications* **15**, 10110 (2024).
23 Li, N. *et al.* Controlling Nucleation Kinetics Via Co-Solvent Strategy for High-Quality Perovskite Films and Large-Area Light-Emitting Diodes. *Small* **21**, e10782 (2025).
24 Deng, Y. *et al.* Surfactant-controlled ink drying enables high-speed deposition of perovskite films for efficient photovoltaic modules. *Nature Energy* **3**, 560-566 (2018).
25 Hu, G. *et al.* A general ink formulation of 2D crystals for wafer-scale inkjet printing. *Science Advances* **6**, eaba5029 (2026).
26 Yu, X. *et al.* "Coffee ring" controlment in spray prepared >19% efficiency Cs0.19FA0.81PbI2.5Br0.5 perovskite solar cells. *Journal of Energy Chemistry* **67**, 201-208 (2022).
27 Liu, Y. *et al.* Fluorescent Microarrays of in Situ Crystallized Perovskite Nanocomposites Fabricated for Patterned Applications by Using Inkjet Printing. *ACS Nano* **13**, 2042-2049 (2019).
28 Tu, Y. *et al.* Fluid-Crystallization Synergy for >26% Efficiency Fully Ambient-Printed SAM-Based Perovskite Photovoltaics. *Advanced Materials* **38**, e73373 (2026).
29 He, M. *et al.* Meniscus-assisted solution printing of large-grained perovskite films for high-

efficiency solar cells. *Nature Communications* **8**, 16045 (2017).
30 Wei, C. *et al.* A Universal Ternary-Solvent-Ink Strategy toward Efficient Inkjet-Printed Perovskite Quantum Dot Light-Emitting Diodes. *Advanced Materials* **34**, 2107798 (2022).
31 Bu, T. *et al.* Lead halide–templated crystallization of methylamine-free perovskite for efficient photovoltaic modules. *Science* **372**, 1327-1332 (2021).
32 Zhang, J., Behringer, R. P. & Oron, A. Marangoni convection in binary mixtures. *Physical Review E* **76**, 016306 (2007).
33 Sun, K. *et al.* Dynamic Reconstruction of Fluid Interface Manipulated by Fluid Balancing Agent for Scalable Efficient Perovskite Solar Cells. *Advanced Materials* **37**, 2419419 (2025).
34 Lee, J.-W. *et al.* Tuning Molecular Interactions for Highly Reproducible and Efficient Formamidinium Perovskite Solar Cells via Adduct Approach. *Journal of the American Chemical Society* **140**, 6317-6324 (2018).
35 Zhang, S. *et al.* Aggregative Luminescence from CsPbBr3 Perovskite Precursors. *Angewandte Chemie International Edition* **63**, e202408586 (2024).
36 Chung, J. *et al.* Engineering Perovskite Precursor Inks for Scalable Production of High-Efficiency Perovskite Photovoltaic Modules. *Advanced Energy Materials* **13**, 2300595 (2023).
37 Liang, Q. *et al.* Manipulating Crystallization Kinetics in High-Performance Blade-Coated Perovskite Solar Cells via Cosolvent-Assisted Phase Transition. *Advanced Materials* **34**, 2200276 (2022).
38 Richter, T., Fricke, M., Stephan, P., Tropea, C. & Hussong, J. Studying macro- and mesoscopic wetting dynamics of a spreading oil droplet using multiple wavelength interferometry. *Experiments in Fluids* **64**, 186 (2023).
39 Bonn, D., Eggers, J., Indekeu, J., Meunier, J. & Rolley, E. Wetting and spreading. *Reviews of Modern Physics* **81**, 739-805 (2009).
40 Wang, J. *et al.* Interfacial Control Toward Efficient and Low-Voltage Perovskite Light-Emitting Diodes. *Advanced Materials* **27**, 2311-2316 (2015).
41 Wang, M., Song, Z., Liu, G. & Wang, D. Entropic Origin of Polymer Nucleation at Amorphous Solid Interfaces. *Physical Review Letters* **135**, 018101 (2025).
42 Pu, W. *et al.* Cost-Effective Acetonitrile-Based Precursor Solution Mitigates Heterogeneous Nucleation for Efficient and Stable Perovskite Solar Cells. *Small* **20**, 2407706 (2024).
43 Zhu, H. *et al.* Retarding Ion Migration for Stable Blade-Coated Inverted Perovskite Solar Cells. *Advanced Materials* **36**, 2306466 (2024).
44 Min, L. *et al.* Carrier dynamic identification enables wavelength and intensity sensitivity in perovskite photodetectors. *Light: Science & Applications* **13**, 280 (2024).
45 Zhao, Y. *et al.* Efficient Perovskite Light-Emitting Diodes by Buried Interface Modification with Triphenylphosphine Oxide. *ACS Applied Materials & Interfaces* **15**, 3644-3650 (2023).
46 D'Innocenzo, V. *et al.* Excitons versus free charges in organo-lead tri-halide perovskites. *Nature Communications* **5**, 3586 (2014).
47 Wang, L. *et al.* Regulated Perovskite Crystallization for Efficient Blue Light-Emitting Diodes via Interfacial Molecular Network. *Advanced Functional Materials* **34**, 2401297 (2024).
48 Zhang, K. *et al.* Top-Down Exfoliation Process Constructing 2D/3D Heterojunction toward Ultrapure Blue Perovskite Light-Emitting Diodes. *ACS Nano* **18**, 4570-4578 (2024).
49 Zhang, X. *et al.* High-performance thermally-evaporated light-emitting diodes via one-step vapor purification. *Light: Science & Applications* **15**, 210 (2026).

50 Liu, Y. *et al.* High-Efficiency and Stable Pure Bromine Blue Light-Emitting Diodes Enabled by Hybrid Quasi-2D Perovskite. *Advanced Functional Materials* **36**, e15841 (2026).

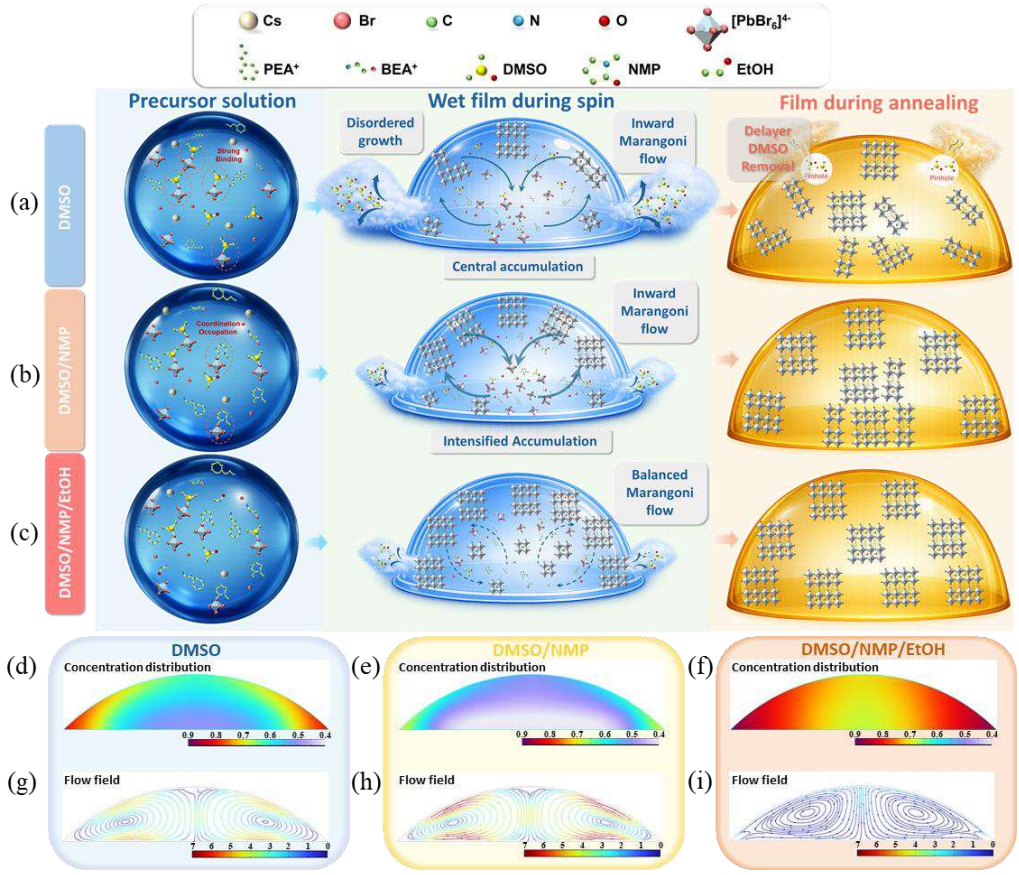

Figure 1. Schematic illustration of precursor solvation, Marangoni-flow-mediated solute redistribution, and annealing crystallization in (a) DMSO, (b) DMSO/NMP, and (c) DMSO/NMP/EtOH systems. Simulated side-view concentration distributions for (d) DMSO, (e) DMSO/NMP, and (f) DMSO/NMP/EtOH systems. Simulated side-view flow-field streamlines for (g) DMSO, (h) DMSO/NMP, and (i) DMSO/NMP/EtOH systems.

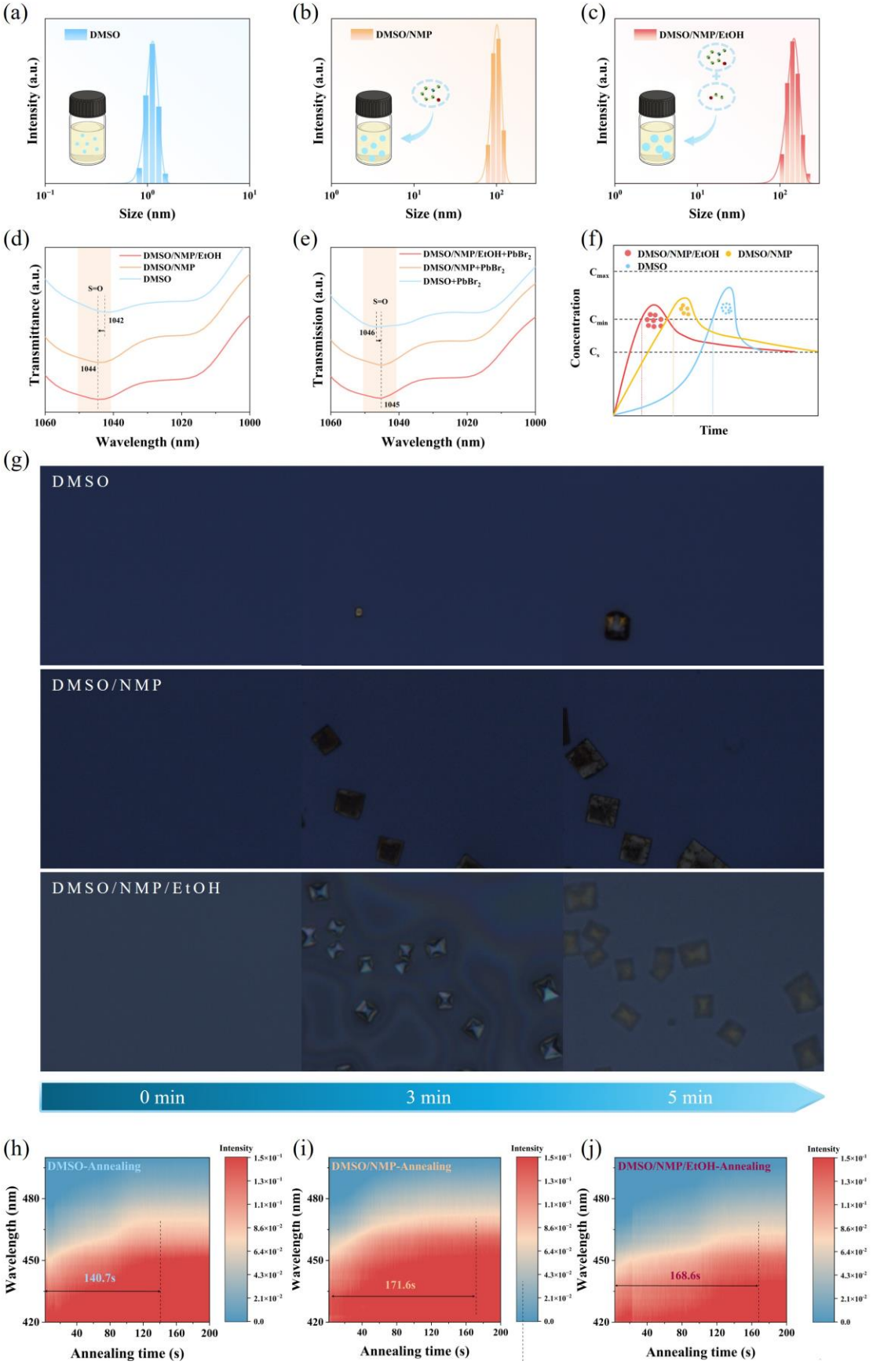
(a)
DMSO
Intensity (a.u.)
Size (nm)
(b)
DMSO/NMP
Intensity (a.u.)
Size (nm)
(c)
DMSO/NMP/EtOH
Intensity (a.u.)
Size (nm)
(d)
DMSO/NMP/EtOH
DMSO/NMP
DMSO
S=O
1042
1044
Transmittance (a.u.)
Wavelength (nm)
(e)
DMSO/NMP/EtOH+PbBr2
DMSO/NMP+PbBr2
DMSO+PbBr2
S=O
1046
1045
Transmission (a.u.)
Wavelength (nm)
(f)
DMSO/NMP/EtOH
DMSO/NMP
DMSO
Cmax
Cmin
Cs
Concentration
Time
(g)
DMSO
DMSO/NMP
DMSO/NMP/EtOH
0 min
3 min
5 min
(h)
DMSO-Annealing
140.7s
Wavelength (nm)
Annealing time (s)
Intensity
(i)
DMSO/NMP-Annealing
171.6s
Wavelength (nm)
Annealing time (s)
Intensity
(j)
DMSO/NMP/EtOH-Annealing
168.6s
Wavelength (nm)
Annealing time (s)
Intensity

759

Figure 2. (a–c) DLS size distributions of perovskite precursor solutions prepared in DMSO, DMSO/NMP, and DMSO/NMP/EtOH, respectively. (d) FTIR spectra of DMSO, DMSO/NMP, and DMSO/NMP/EtOH. (e) FTIR spectra of $PbBr_2$ dissolved in DMSO, DMSO/NMP, and DMSO/NMP/EtOH. (f) Schematic LaMer model illustrating nucleation and crystal growth in DMSO, DMSO/NMP, and DMSO/NMP/EtOH systems. (g) In situ optical microscopy images showing nucleation and crystal growth in different solvent systems. (h–j) 2D contour maps of in situ UV–vis absorption spectra of perovskite films prepared from DMSO, DMSO/NMP, and DMSO/NMP/EtOH, respectively, during annealing.

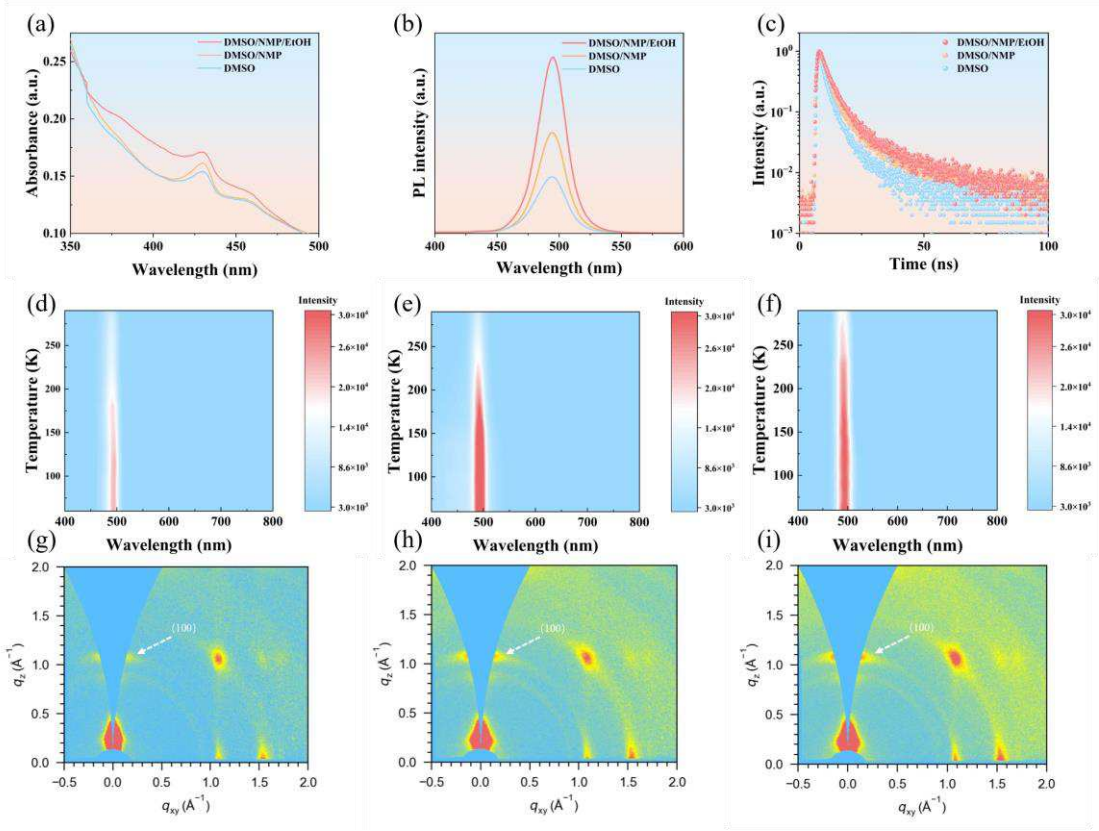

Figure 3. (a) UV–vis absorption spectra of annealed perovskite films prepared from three different solvent systems. (b) Steady-state PL spectra (excitation: 365 nm). (c) TRPL spectra of perovskite films deposited on glass substrates. (d–f) 2D temperature-dependent PL maps (60–290 K, excitation: 365 nm) of perovskite films prepared from DMSO, DMSO/NMP, and DMSO/NMP/EtOH, respectively. (g–i) 2D GIWAXS patterns of perovskite films prepared from DMSO, DMSO/NMP, and DMSO/NMP/EtOH, respectively.

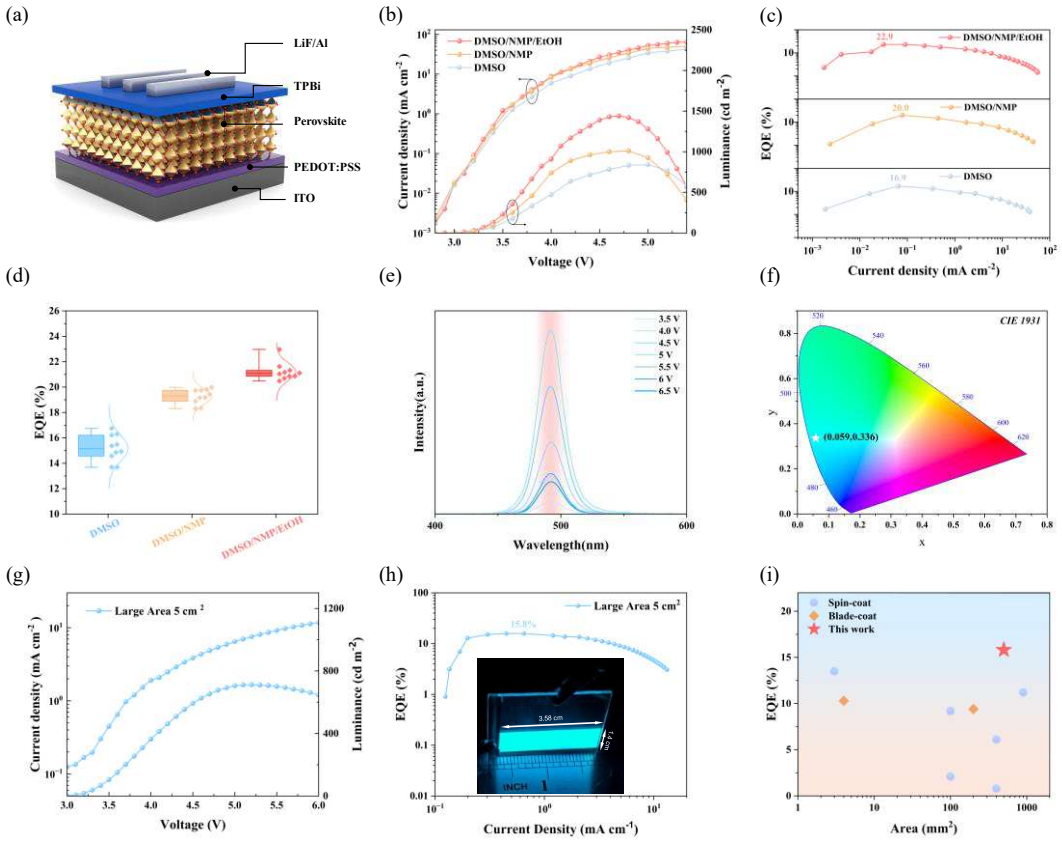

Figure 4. (a) Schematic device structure of blue PeLEDs. (b) J–V–L characteristic curves. (c) EQE–J characteristic curves. (d) EQE box plots with individual data points. (e) Voltage-dependent EL spectra. (f) CIE 1931 chromaticity coordinates of the DMSO/NMP/EtOH-based devices. (g) J–V–L characteristics and (h) EQE–J curve (inset: photograph of the operating device) of large-area PeLEDs with an active area of 5 cm². (i) Comparison of peak EQE and active area between this work and previously reported large-area blue PeLEDs.

ToC

A coordination–hydrodynamic synergy couples DMSO/NMP/EtOH solvent chemistry with Marangoni flow balancing to direct uniform crystallization of sky-blue perovskite films. NMP promotes nucleation via solvation control, while EtOH enables solute redistribution via Marangoni counterflow. This yields 22.9% EQE (0.1 cm²) and 15.8% EQE over 5 cm²—among the best for large-area blue PeLEDs.

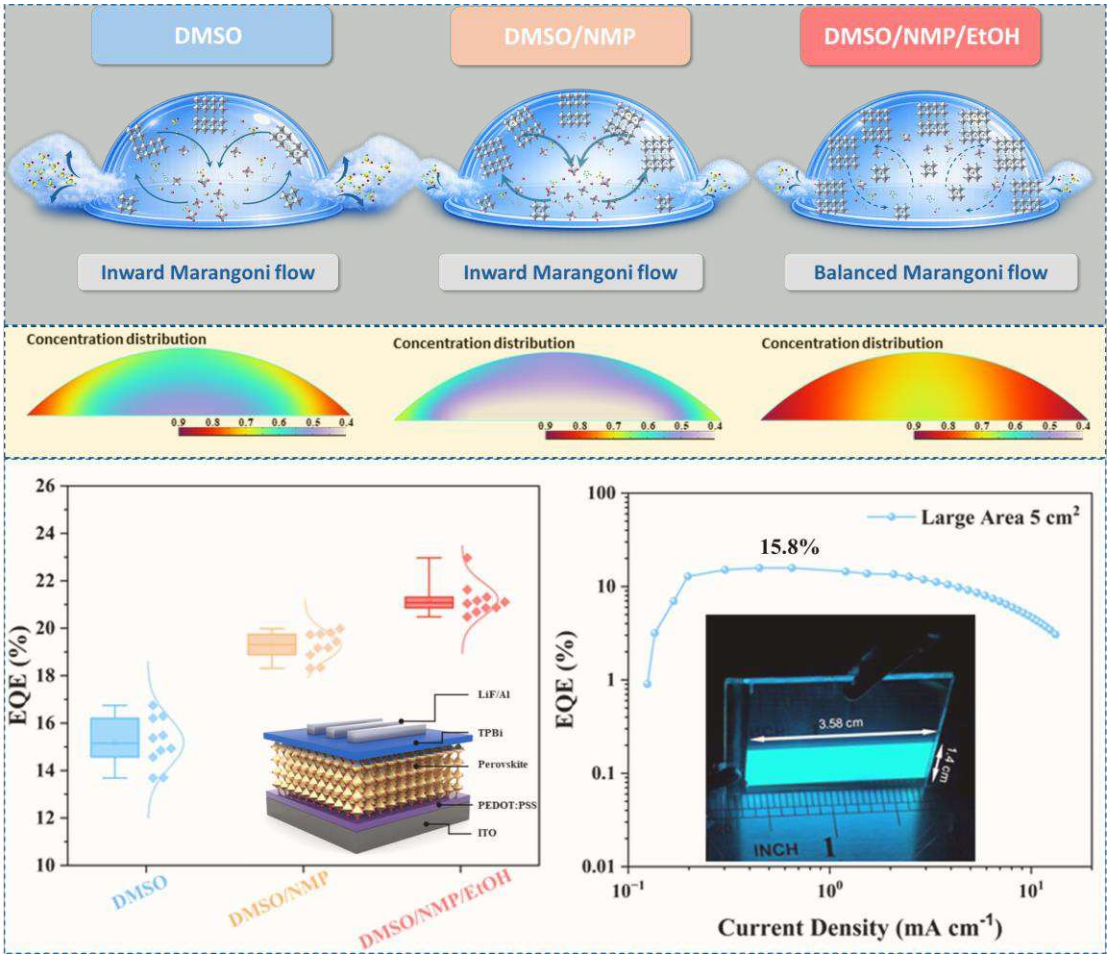

Supplementary Files

This is a list of supplementary files associated with this preprint. Click to download.

- YangLSASI.pdf